Nanoscale Horizons

ROYAL SOCIETY OF CHEMISTRY

COMMUNICATION

View Article Online
View Journal | View Issue

Cite this: *Nanoscale Horiz.*, 2024, **9**, 1948

Received 17th June 2024,
Accepted 27th August 2024

DOI: 10.1039/d4nh00282b

rsc.li/nanoscale-horizons

Graphene-based microelectrodes with bidirectional functionality for next-generation retinal electronic interfaces†

Fikret Taygun Duvan,[a] Marina Cunquero,[b] Eduard Masvidal-Codina,[a] Steven T. Walston,[a] Maria Marsal,[b] Jose Manuel de la Cruz,[a] Damia Viana,[a] Diep Nguyen,[c] Julie Degardin,[c] Xavi Illa,[de] Julie M. Zhang,[c] Maria del Pilar Bernícola,[a] José Gabriel Macias-Montero,[f] Carles Puigdengoles,[f] Gustavo Castro-Olvera,[b] Elena del Corro,[a] Socrates Dokos,[g] Mokhtar Chmeissani,[f] Pablo Loza-Alvarez,[b] Serge Picaud[c] and Jose A. Garrido*[ah]

Neuroelectronic prostheses are being developed for restoring vision at the retinal level in patients who have lost their sight due to photoreceptor loss. The core component of these devices is the electrode array, which enables interfacing with retinal neurons. Generating the perception of meaningful images requires high-density microelectrode arrays (MEAs) capable of precisely activating targeted retinal neurons. Achieving this precision necessitates the downscaling of electrodes to micrometer dimensions. However, miniaturization increases electrode impedance, which poses challenges by limiting the amount of current that can be delivered, thereby impairing the electrode's capability for effective neural modulation. Additionally, it elevates noise levels, reducing the signal quality of the recorded neural activity. This report focuses on evaluating reduced graphene oxide (rGO) based devices for interfacing with the retina, showcasing their potential in vision restoration. Our findings reveal low impedance and high charge injection limit for microscale rGO electrodes, confirming their suitability for developing next-generation high-density retinal devices. We successfully demonstrated bidirectional interfacing with cell cultures and explanted retinal tissue, enabling the identification and modulation of multiple cells' activity. Additionally, calcium imaging allowed real-time monitoring of retinal cell dynamics, demonstrating a significant reduction in activated areas with small-sized electrodes. Overall, this study lays the groundwork for developing advanced rGO-based MEAs for high-acuity visual prostheses.

New concepts

The study introduces an innovative approach in the field of retinal prostheses by employing reduced graphene oxide (rGO) microelectrode arrays (MEAs) for high-resolution bidirectional interfacing with retinal cells. Unlike traditional metal-based microelectrodes, rGO microelectrodes offer significant advantages due to their low impedance and high charge injection limits. These features are crucial for reducing the size of electrodes while maintaining effective stimulation and recording capabilities, enabling more precise activation of targeted retinal neurons. The bidirectional functionality allows for real-time monitoring and modulation of retinal cell activity, with potential implications for closed-loop applications. By demonstrating a scalable method to fabricate high-performance microelectrodes, the work presents a robust rGO-based technology for retinal vision restoration.

1 Introduction

Brain–machine interfaces are expected to revolutionize rehabilitation strategies, particularly for sensory restoration. While auditory prostheses have achieved significant success, visual prostheses are still in the early stages of development. Retinal vision restoration requires replication of real-world images composed of many pixels, necessitating a high density of electrodes to be implanted in the macular area. Retinal prostheses are designed to restore vision in blinding diseases associated with photoreceptor degeneration, such as retinitis

[a] *Catalan Institute of Nanoscience and Nanotechnology (ICN2), CSIC and BIST, Campus UAB, Bellaterra, Spain. E-mail: joseantonio.garrido@icn2.cat*
[b] *Institut de Ciències Fotòniques (ICFO), The Barcelona Institute of Science and Technology, Castelldefels, Spain*
[c] *Institut de la Vision, Sorbonne Université, INSERM, CNRS, Paris, France*
[d] *Institut de Microelectrònica de Barcelona, IMB-CNM (CSIC), Campus UAB, Bellaterra, Spain*
[e] *Centro de Investigación Biomédica en Red de Bioingeniería, Biomateriales y Nanomedicina, Instituto de Salud Carlos III, Bellaterra, Spain*
[f] *Institut de Física d'Altes Energies (IFAE), BIST, Campus UAB, Bellaterra, Spain*
[g] *Graduate School of Biomedical Engineering, The University of New South Wales Sydney, Sydney, NSW, Australia*
[h] *Institució Catalana de Recerca i Estudis Avançats (ICREA), Barcelona, Spain*

† Electronic supplementary information (ESI) available. See DOI: https://doi.org/10.1039/d4nh00282b

pigmentosa (RP) and age-related macular degeneration (AMD). In both pathologies, photoreceptors in the outer layer of the retina are gradually lost, while neurons in the inner retina remain functional despite undergoing some remodeling.[1–3] Retinal prostheses mimic photoreceptor function by stimulating the remaining retinal circuit *via* electrical current injection. This leads to the excitation of retinal ganglion cells (RGCs), which convey this information to the brain through the optic nerve. Such electrical stimulations of the residual retinal circuitry were found to elicit the perception of visual percept or phosphenes.[4] Their proper spatial distribution can generate form or letter perception.[5,6]

Three main intervention strategies are employed in retinal prosthetics for establishing interfaces with retinal neurons: epiretinal, subretinal, and suprachoroidal approaches.[7] The epiretinal approach involves the placement of a device on the innermost surface of the retina, offering direct proximity to RGCs and facilitating a relatively straightforward surgical procedure. The subretinal approach utilizes the space between the retinal pigment epithelium and bipolar cells in efforts to capitalize on the retinal circuitry's remaining preprocessing capabilities. Finally, the suprachoroidal technique interfaces with the retina from the space between the sclera and choroid of the eye and is distinguished by its minimally invasive nature. Various vision-restoring devices have been developed and tested clinically, such as the Argus II by Second Sight Medical Products (Sylmar, USA),[8] IRIS II[9] and PRIMA[10] from Pixium Vision (Paris, France), and Alpha IMS from Retina Implant AG (Reutlingen, Germany).[11]

The efficacy of these prosthetic approaches relies heavily on their ability to deliver targeted, focal electrical stimulation. Ideally, focal stimulation would activate only the neuron somas in close proximity to the stimulating electrode, thereby generating focused phosphenes. By integrating individual phosphenes generated by multiple electrodes, a complex and coherent perception of shapes, such as letters, becomes possible.[5] However, achieving this has been challenging due to several factors: unintended axonal activation,[12] the large size and low density of electrodes, which lead to extensive current spread;[13] desensitization of retinal ganglion cells (RGCs) to repetitive stimulation;[14] and the variability in perception thresholds across patients as well as among individual electrodes within the same patient.[15,16]

Extensive efforts have been directed towards optimizing stimulation patterns and paradigms. Weitz and colleagues[17] demonstrated focal stimulation by using small electrodes and long pulse widths in order to avoid unintended activation. The impact of different pulse widths and shapes, stimulation amplitudes and frequencies, and employment of current steering methods has been widely explored.[18–22] Furthermore, the necessity of real-time parameter optimization to avoid unwanted axonal activation, as well as compensating for patient-to-patient variability, is becoming increasingly apparent.[23] Achieving this optimization is likely to be more feasible with high-density microelectrode arrays (MEAs) capable of both recording and stimulation.

In the realm of retinal vision restoration, the current state of clinically tested devices has yet to achieve visual acuity surpassing the legal blindness threshold of 1/20. However, the improvement in visual acuity over the last three decades was related to a decrease in the electrode size from 200 μm in the Argus II implant, 250 μm in the Iris II device to 50 × 50 μm in the Alpha AMS and 30 μm in the PRIMA device. This reduction in the size of individual electrodes was made possible by the development of innovative electrode materials, from platinum in the Argus II to sputtered iridium oxide (SIROF) in the Alpha AMS and PRIMA devices.[24] Further reduction in electrode dimensions is limited by the electrode material, which affects intrinsic recording noise and the safe charge injection limit. To elicit action potentials *in vitro*, mammalian retinas typically require charges between 0.15–0.3 mC cm^{-2}.[25] In chronic *in vivo* conditions, however, the required charge can exceed this by more than tenfold,[26] necessitating materials with a high CIL.

Nanoporous materials, such as reduced graphene oxide (rGO), show promise in this area, offering charge injection limit (CIL) of up to 5 mC cm^{-2} and enabling bidirectional neural interfacing with neurons, as we have previously reported.[27] In this context, rGO is more advantageous than single-layer graphene due to its stacked flake structure, which facilitates higher double layer capacitance and charge injection capacity. We developed and evaluated rGO MEAs for recording and modulation of retinal cell activity. We conducted extensive electrochemical characterization to assess their performance. Functionality tests with neural cultures were carried out to record electrical activities and investigate the effects of different stimulation parameters. Subsequently, we tested these electrodes with retinal explants, successfully demonstrating their capability for single-unit recordings and modulation of retinal activity. The use of calcium imaging offered valuable insights into neuronal activity and response dynamics under various stimulation scenarios.

2 Results & discussion

2.1 Fabrication and electrochemical characterization of rGO MEAs

Free-standing GO films were obtained by vacuum filtration of GO flakes suspended in an aqueous solution, which were then transferred onto the final substrate and hydrothermally reduced. Electrode geometries were patterned and passivated to obtain arrays of rGO microelectrodes (n = 60) with diameters of 25 μm, 50 μm, and 100 μm as shown in Fig. 1a (see Experimental for details). The thickness of the active site of the finalized rGO microelectrodes was approximately 2 μm, as characterized by SEM (Fig. 1b), showing the volumetric nature of our electrodes. AFM measurements showed a maximum surface roughness of about 0.6 nm (R.M.S.), as given in Fig. 1c, left panel. A representative Raman spectrum of an rGO microelectrode is shown in the right panel of Fig. 1c, where the characteristic peaks of rGO (D ≃ 1350 and G ≃ 1589 cm^{-1}) are visible, revealing a $I_{D/G}$ ratio of 1.14 after the hydrothermal reduction.[27]

The electrochemical characterization of the rGO electrodes is detailed in Fig. 2. Bode plots of the impedance spectra are

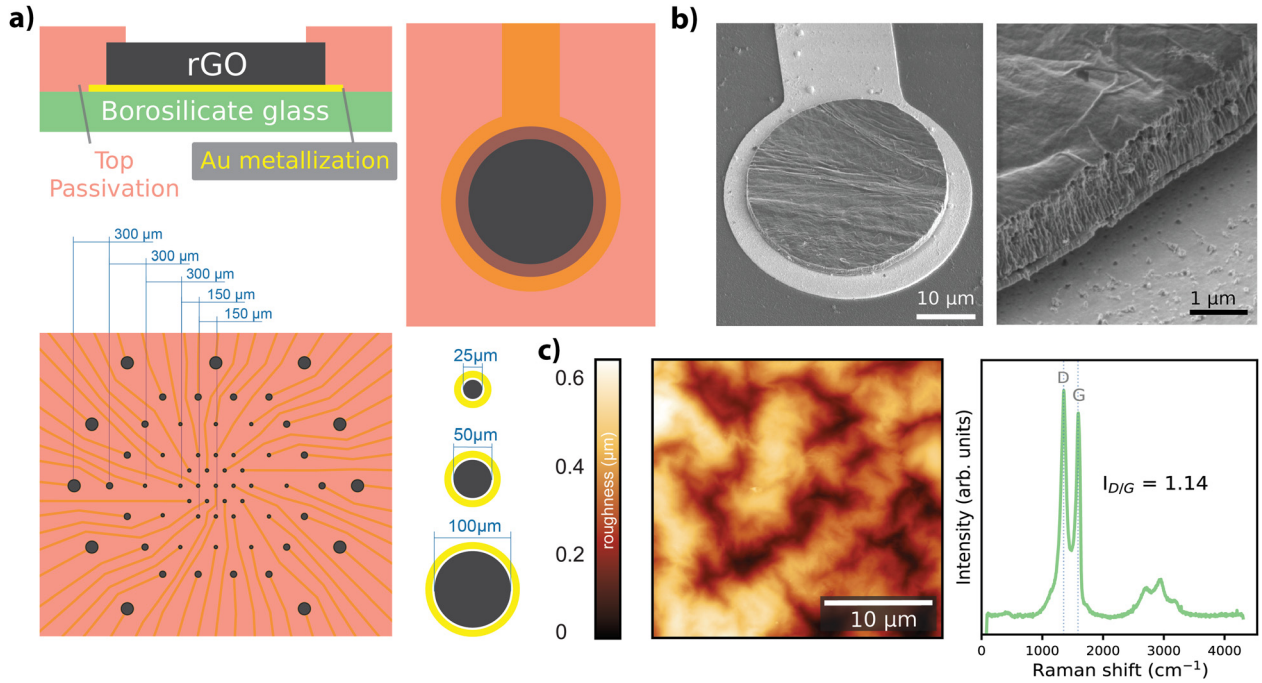

Fig. 1 Fabrication and characterization of rGO MEAs. (a) Cross-section and top views of a microelectrode from the array, bottom panel shows the MEA design together with size and pitch of the electrodes. (b) SEM images showing the structure of a single microelectrode and the cross-section of the rGO structure before deposition of the top passivation layer. (c) Representative AFM image (left) and Raman spectrum (right) of the rGO microelectrode.

featured in Fig. 2a for electrodes with diameters of 25 µm, 50 µm, and 100 µm. The averaged impedance magnitudes (measured at 1 kHz) grouped by electrode size were 27.6 ± 2.97 kΩ (n = 32, 25 µm), 11.9 ± 0.44 kΩ (n = 24, 50 µm), and 6.37 ± 0.43 kΩ (n = 25, 100 µm). An inverse relationship between impedance and frequency can be observed, with phase angle reaching −80° (see Fig. 2a), characteristic of a non-ideal capacitor. This trend is consistent up to the lower hundreds of Hz, beyond which the resistance of the solutions becomes more prominent, leading the phase to approach 0 degrees, indicative of a purely resistive response. The capacitive regime reflects the ability of our electrodes to store charge in the electrochemical double layer, as discussed elsewhere.[27]

To better understand the frequency response of rGO microelectrodes, we developed a simple, lumped-element equivalent circuit model. The model includes a fixed resistor R_0, set at 10 Ω, and a set of parallel resistor (R) and capacitor (C) pairs arranged in a transmission line-like configuration, as depicted in Fig. 2b. The results from the impedance magnitude fitting for 25 µm electrode data, depicted in Fig. 2a with dashed lines, reveal a close match with the measured data. However, for the phase, particularly at low frequencies, a deviation resulting from the use of RC pairs is visible. Fitting results for the remaining electrode diameters showed similar dynamics, as depicted in Fig. S1a (ESI†), along with the normalized root mean square error (NRMSE) for the fits (Fig. S1b, ESI†).

The model serves as a theoretical framework, bridging the gap between measured observations and a deeper understanding of the underlying electrochemical processes. We intentionally avoided the use of a constant phase element (CPE), commonly used in modelling non-ideal capacitive behaviour, due to the complexities involved.[28] Our modelling strategy offers a simplified integration into time domain modelling using finite element method (FEM) software. The accuracy of the model is found to be adequate for approximating the frequency response of our electrodes, as shown by the low error values (see Fig. S1b, ESI†). Further development of the model will aid in the design of more effective neural interfaces.

We then studied the current density achieved under cyclic voltammetry with a 50 mV s^{-1} scan rate. The highest current densities were achieved with the smallest diameter electrodes (Fig. 2c). Cathodic charge storage capacity (CSC_C) for the different size groups was calculated from the integral of the CV curves.[29,30] Similar to the observation for the current density, the CSC_C values varied significantly with the different electrode diameters: 38.44 ± 7.16 mC cm^{-2} for 25 µm, 18.92 ± 1.85 mC cm^{-2} for 50 µm, and 11.78 ± 1.41 mC cm^{-2} for 100 µm (Fig. 2d). This dependence of electrochemical performance on electrode area has been previously reported for other materials, and is generally attributed to diffusion-limited ionic transport.[29,31,32]

Next, we focused on assessing the CIL of the electrodes, a critical parameter for their application in neural interface technology. For clarity, it should be noted that while the terms 'charge injection capacity' and 'charge injection limit' are used interchangeably in the literature, in this paper, we will consistently refer to it as CIL. Chronoamperometry measurements for a 25 µm electrode, using cathodic first charge-balanced biphasic current injections with 1 ms pulse width and amplitudes ranging from 5 to 20 µA, are illustrated in Fig. 2e. Capacitive polarization across the electrode–liquid interface was

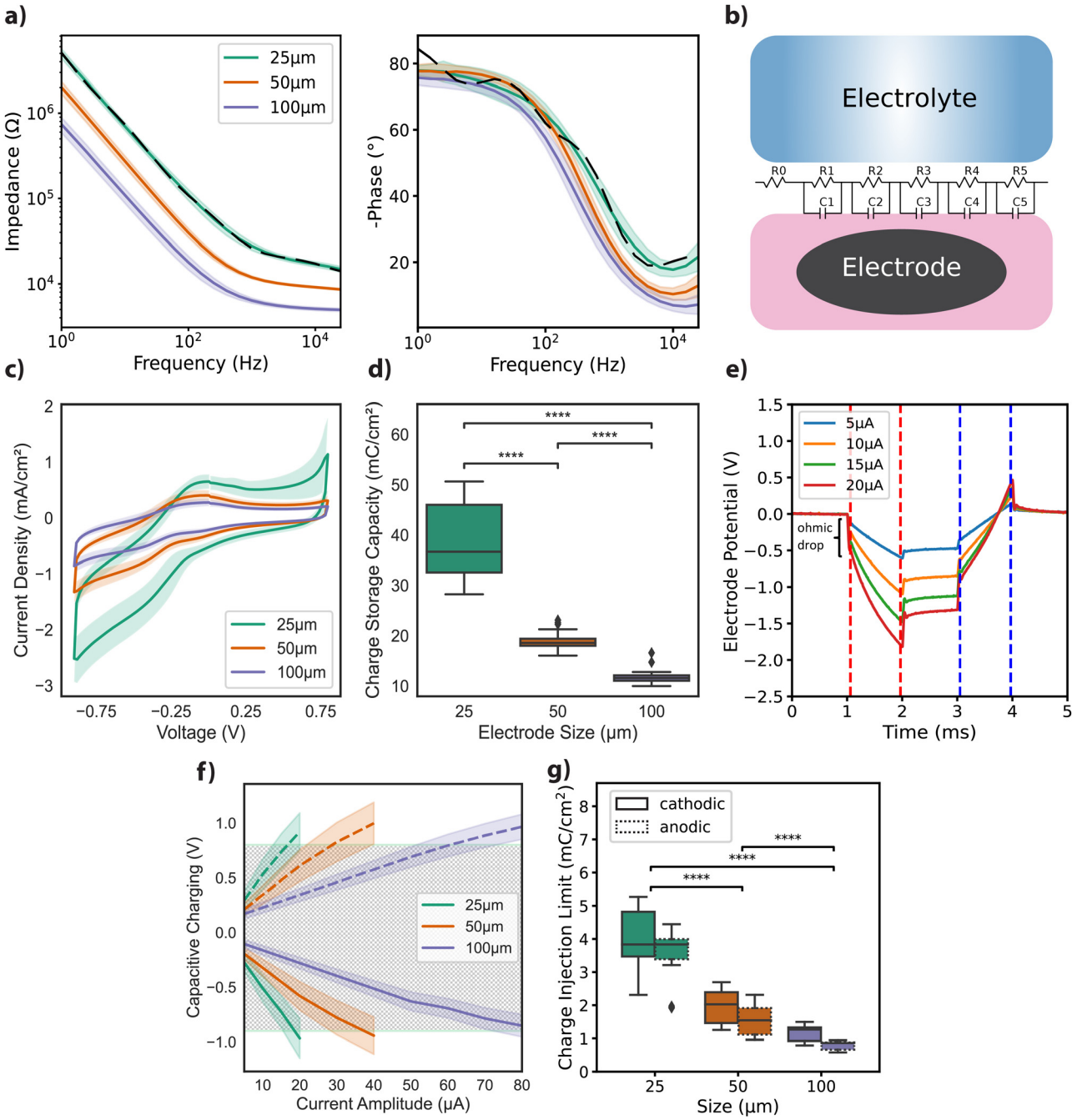

Fig. 2 Electrochemical characterization of rGO electrodes. (a) Impedance spectra of the electrodes in Bode plot form, (left) magnitude and (right) phase for 25 µm (n = 32, shown in green), 50 µm (n = 24, orange), and 100 µm (n = 25, purple) diameter electrodes. The dashed lines represent fitting of the model detailed in panel b to the data of 25 µm electrodes. Shaded regions depict standard deviation. (b) Equivalent circuit model (based on lumped elements) for the electrode interface. (c) Averaged cyclic voltammetry traces for 25, 50, and 100 µm diameter electrodes, depicted by current densities *versus* potential (scan rate: 50 mV s^{-1}). Shaded regions show standard deviation. (d) CSCc extracted from the CV curves depicted in (c). Statistical test (Mann–Whitney–Wilcoxon, ****: $p < 10^{-4}$). (e) Voltage excursions recorded in response to 1 ms charge-balanced biphasic pulses with 1 ms inter-phase gap of varying amplitudes (5–20 µA) for a 25 µm electrode. (f) Polarization across the interface for cathodic (solid lines) and anodic (dashed lines) charging for the different size groups. The chequerboard area represents the electrochemical window determined by CV measurements. (g) Boxplots of cathodic (solid boxes) and anodic (dashed boxes) charge injection limits for each size group (Mann–Whitney–Wilcoxon, ****: $p < 10^{-4}$).

calculated by extracting voltage excursions after the ohmic drop for both the cathodic (red dashes) and anodic (blue dashes) phases (Fig. 2e). From the plot of capacitive polarization against injected current amplitudes (see Fig. 2f), we calculated the following CIL averages for electrodes grouped by diameter: 3.94 ± 0.85 mC cm^{-2} (cathodic) and 3.52 ± 0.74 mC cm^{-2} (anodic) for 25 µm microelectrodes; 1.96 ± 0.47 mC cm^{-2} (cathodic) and 1.55 ± 0.42 mC cm^{-2} (anodic) for 50 µm

microelectrodes; 1.17 ± 0.22 mC cm^{-2} (cathodic) and 0.79 ± 0.12 mC cm^{-2} (anodic) for 100 μm microelectrodes, as depicted in Fig. 2g.

To further contextualize our findings, we considered relevant literature on electrode performance. Comparative studies demonstrate a broad range of CIL and impedance values across different materials and electrode designs. For instance, a CIL of 0.9 mC cm^{-2} for TiN and 5.75 mC cm^{-2} for iridium oxide (IrOx) has been documented for electrodes with a 4000 μm^2 surface area, using 0.5 ms anodic pulses.[31] Additionally, surface treatments on platinum wire electrodes (d = 0.5 mm) have been shown to increase CIL up to 1 mC cm^{-2} using 400 μs biphasic pulses.[33] SIROF electrodes have displayed impedance values ranging from 12 ± 1.4 kΩ to 241 ± 11 kΩ for surface areas between 1960 μm^2 and 20 μm^2. The CIL using 1 ms biphasic pulses was calculated as 4 mC cm^{-2} and 3.4 ± 0.05 mC cm^{-2} (n = 4) for electrodes measuring 95 μm^2 and 1960 μm^2,[32] comparable to our findings. An impedance around 20 kΩ at 1 kHz has been reported for 30 μm diameter PEDOT:CNT electrodes, along with a CIL above 1 mC cm^{-2} measured by biphasic, anodic-first, voltage pulses of 700 mV amplitude.[34] In a study by Wilks *et al.*, the following impedance values (at 1 kHz) were reported for 15 μm diameter electrodes: 404.5 ± 15.2 kΩ for iridium (Ir), 113.6 ± 3.5 kΩ for IrOx, and 23.3 ± 0.7 kΩ for PEDOT:PSS. They also noted charge storage capacities for IrOx electrodes of 28.8 ± 0.3 mC cm^{-2} at 50 mV s^{-1} and 17.6 ± 0.2 mC cm^{-2} at 1 V s^{-1}. For PEDOT:PSS electrodes, they reported charge storage capacities of 75.6 ± 5.4 mC cm^{-2} and 178.5 ± 5.3 mC cm^{-2}, for the two scan rates, respectively. Additionally, the CIL for 23 μm PEDOT:PSS electrodes was determined to be up to 3.45 mC cm^{-2} using cathodic-first biphasic pulses of 200 μs.[35] A study by Green and colleagues[36] reported the CIL for 380 μm diameter electrodes. PEDOT-coated Pt electrodes demonstrated a CIL of 3.90 mC cm^{-2} in PBS and 2.60 mC cm^{-2} in serum-loaded cell culture medium. In comparison, bare Pt electrodes showed a CIL of 0.12 mC cm^{-2} in PBS and 0.007 mC cm^{-2} in media, using cathodic-first biphasic pulses of 800 μs. These data suggest that rGO electrodes are among the best performers (see ref. 32, 37 and 38 for extended CIL comparisons between various materials).

The mechanical stability and biocompatibility of rGO had been demonstrated in a previous study,[27] where chronic implantation of microelectrodes in rodent brains resulted in minimal inflammation and stable tissue integration. The electrodes maintained their structural integrity and performance through sonication and bending tests, and electrochemical impedance remained stable after continuous electrical stimulation, confirming their mechanical robustness and reliability.

2.2 Hippocampal cultures for functional testing

The recording capabilities of the rGO MEAs were evaluated by cultivating hippocampal neurons directly on the devices and subsequently recording spontaneous electrical activity within the cell culture (see Fig. S2 for description of the experimental setup, ESI†). Progression of hippocampal cell growth over a 2-week period on rGO MEAs is depicted in Fig. 3a. At 4 days *in vitro* (DIV), the cells start forming the neurites and by 12 DIV, the neurons have established a mature network. Spontaneous activity recorded by electrodes of different diameters confirmed the viability of the cultured cells as shown in Fig. 3b, along with averaged spike shapes across the recording (see Fig. S3a and b for extended comparisons, ESI†). The noise floor and peak-to-peak amplitudes V_{p-p} of the spiking activity are observed to depend on the electrode size. The amplitude of the recorded neural activity was found to vary between 10 and 100 μV, with smaller diameter electrodes capturing larger spike amplitudes. Specifically, V_{p-p} averages were calculated as 53.56 ± 25.92 μV (n = 13) for 25 μm electrodes, 36.09 ± 9.5 μV (n = 13) for 50 μm electrodes, and 19.32 ± 1.71 μV (n = 8) for 100 μm electrodes. The signal-to-noise ratio (SNR) was calculated for each channel, as detailed in the Experimental section, considering only channels where spontaneous neural activity was detected. SNR values, mapped onto the electrode layout, are displayed in Fig. S3c (ESI†). Average SNR measurements for electrodes sized 25 μm, 50 μm, and 100 μm are 24.74 ± 2.52 dB, 24.36 ± 1.16 dB, and 23.02 ± 0.56 dB, respectively, and are illustrated in Fig. 3c. There were no significant differences in SNR between the size groups, although the smaller electrodes recorded higher amplitude signals. This is attributed to smaller electrodes also having a higher noise floor.

Our observation regarding the start of the spontaneous activity due to maturation of the neural network around DIV 13, has previously been reported.[39,40] Nam and colleagues employed TiN-based MEAs of comparable size (30 μm), reporting mean extracellular spike amplitudes of 25 μV at 7 DIV and 50 μV at 20–24 DIV, which fits well with our observations. Similar to our results, Camunas and colleagues observed that signal amplitude is inversely proportional to electrode dimensions.[41] Furthermore, it has been proposed that electrodes with diameters exceeding 50 μm may exhibit a lower signal-to-noise ratio (SNR) by causing a dispersal of the neuron's peak signal, effectively averaging it out.[42] Our results, however, do not show any significant difference in SNR between the electrode sizes, although the V_{p-p} values from some channels were noticeably different (Fig. 3b). It is important to note that there is no consensus in the literature regarding the computation of SNR values,[43,44] which makes it challenging to directly compare SNR values across different studies.

Subsequently, we tested the neuromodulation capabilities of rGO MEAs by recording responses from dissociated hippocampal cultures to voltage pulses of varying widths and amplitudes. The effects of varying the voltage amplitude while keeping the pulse width at 900 μs are shown in Fig. 3d. We also tested pulse widths while keeping the pulse amplitude fixed at 900 mV (Fig. S3d, ESI†). The spiking activity, represented by the density and distribution of points in the raster plot, along with the corresponding spike count histogram, indicates a clear modulation of firing rate in response to changes in voltage amplitude. This suggests that the neurons exhibit differential sensitivity to the amplitude of stimulation, which is critical for the fine-tuning of excitability in neural circuits. The bidirectional nature of the system is highlighted by its ability to not

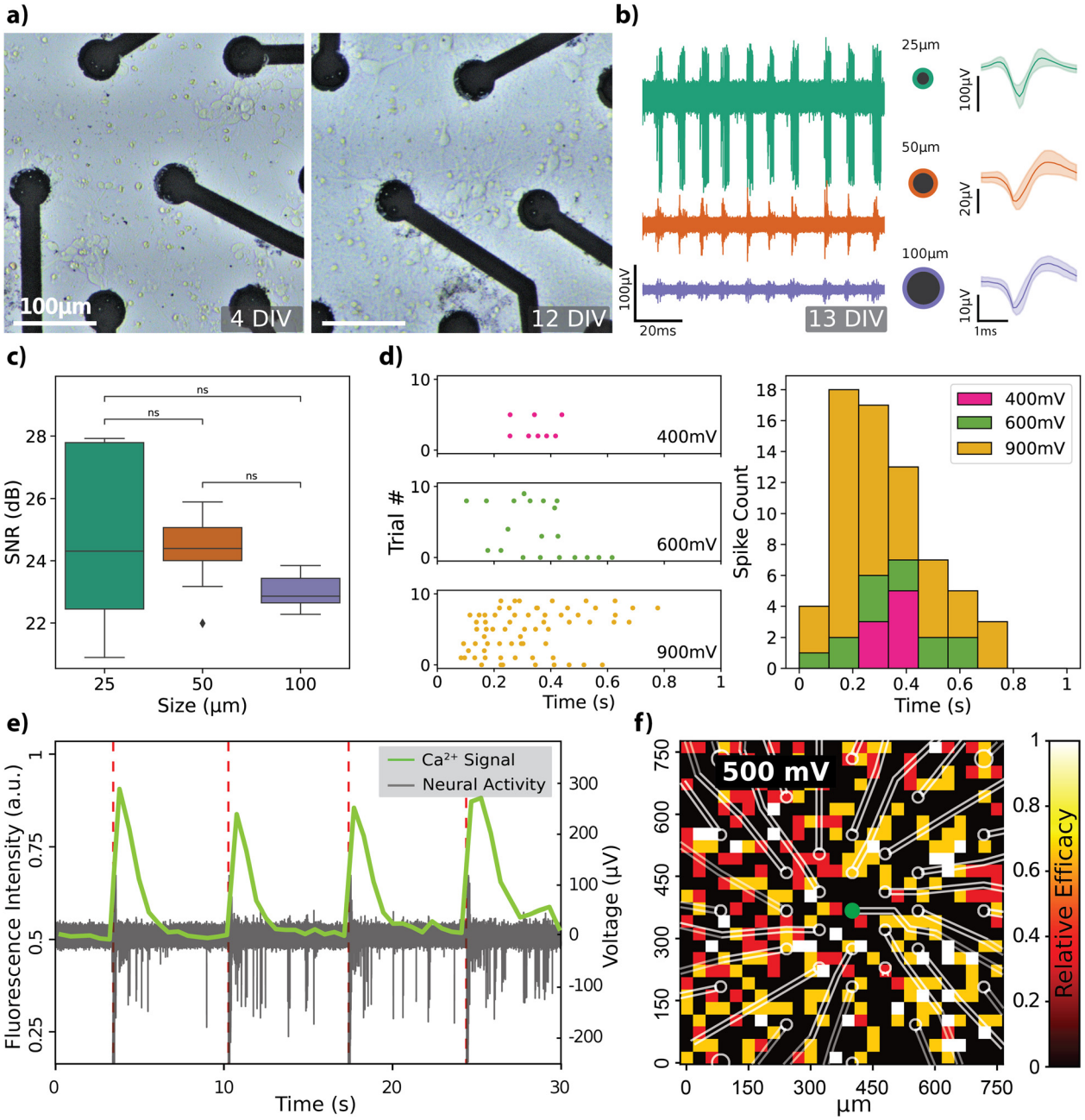

Fig. 3 Functional characterization of rGO MEAs employing hippocampal neurons in culture. (a) Images of neuronal network maturation during 12 DIV. The scale bars represent 100 µm. (b) Neural activity recorded by 25 µm (green), 50 µm (orange), and 100 µm (purple) diameter electrodes at DIV 13. (c) Average SNR by electrode size as calculated from channels where spontaneous activity is observed (one-way ANOVA: n.s.). (d) Modulation effects of varying the voltage amplitude on neural activity (stimulation and recording at the same electrode, 25 µm). Left panel: Raster plots depict the spikes generated in each trial with a given stimulation amplitude. Right panel: Histogram depicts the spike counts from different amplitudes. (e) Simultaneous recording of electrical activity and change in fluorescence intensity in response to injections of 650 mV, 500 µs biphasic pulses (depicted in dashed red lines). (f) Relative stimulation efficacy shown as a grid plot, in response to 500 mV, 500 µs stimulation. Green dot shows the stimulation electrode.

only record neuronal activity but also to actively modulate it through electrical stimulation.

The transparent substrate of the rGO MEA design enabled simultaneous calcium imaging as a complementary method for spatially observing hippocampal neuron responses. Fig. 3e shows responses to a single voltage-controlled biphasic pulse of 650 mV amplitude and 500 µs pulse width. The stimulus elicited the firing of action potentials, which is correlated with an increase in the fluorescence intensity of the calcium indicator. To test how stimulation with a single 25 µm electrode affected the total response in the field of view, we measured the relative stimulation efficacy (RSE) while varying the voltage amplitude. This measure is calculated by dividing the count of stimuli that elicited a spike by the total number of stimuli

administered (see Experimental). Grid plot of RSE in response to voltage-controlled stimuli of 500 mV with a 500 μs pulse width is shown in Fig. 3f. Effects of the voltage amplitude on the spatial response is further depicted on Fig. S3e (ESI†) where stimuli of 250 mV generated weak response whilst 350 mV generated a response of 0.5 RSE that covered the full field of view. When increasing the voltage from 350 mV to 500 mV the intensity and spread of response increased.

2.3 Modulation of neural activity in *ex vivo* retinas

Retinal explants from Long-Evans rats were flat-mounted on the rGO MEAs by positioning the RGC layer directly on top of the electrodes (see Experimental), to evaluate the bidirectional interfacing capabilities of the rGO MEAs in an environment relevant for vision restoration applications. First, in order to assess the functionality of the experimental setup, which incorporated retinal explants, light-evoked action potentials were recorded from retinal neurons. From these recordings, we identified 56 distinct neural units with response amplitudes ranging from 20 to 100 μA. Spike shapes are displayed in Fig. 4a; each unit in a given channel is represented by a different colour, highlighting the multiple spiking signatures observed on some channels.

We categorized the neural response dynamics of these neurons into 'ON' or 'OFF' responses, based on their activity in relation to the stimulus state. Fig. 4b illustrates this concept through a raster plot (middle panel) and *peri*-stimulus time histogram (PSTH) (bottom panel), which display the responses of two units recorded by the same channel. Each unit exhibits distinct response characteristics: cell 1 maintains sustained activity throughout the light stimulus, whereas cell 2 demonstrates transient responses at both the onset and the offset of the stimulus. To validate the biological origin of the observed responses, we used a metabotropic glutamate receptor agonist L-AP4, which is known to interfere with the retinal ON signalling pathway, blocking the corresponding ON response from RGCs.[45] A comparison of the response from the same cell before and after L-AP4 perfusion shows selective blockade of the ON-type response (see Fig. S4a, ESI†), confirming the biophysical origin of the recorded action potentials.

Next, we tested the stimulation capability of the MEAs using biphasic current pulses of varying amplitudes and pulse widths (complete set of parameters given in Table S1, ESI†). Fig. 4c depicts representative responses to charge-balanced biphasic current pulses with a pulse width of 500 μs and two different current amplitudes (see Fig. S4b for the extended version, ESI†). These trials were recorded by an electrode (25 μm diameter) located 150 μm laterally to the stimulation electrode (also 25 μm diameter). Due to stimulation artefact removal, a blind period of a few milliseconds post-stimulation is evident, appearing as a flat line in the recording. The response characteristics, notably the total spike count, exhibited a scaling effect based on the stimulation amplitude. This trend remained consistent across the spectrum of explored amplitudes and pulse widths.

To benchmark our MEAs against existing literature, we analysed the temporal dynamics of the retinal responses with respect to stimulation, categorizing them into light-ON, light-OFF, and electrical stimulation responses (see Fig. 4d). We observed an average delay of 130 ± 60 ms (n = 45) for the ON-type and 80 ± 30 ms (n = 48) for the OFF-type first spiking latencies; peak spiking latencies were 215 ± 74 ms for ON-type and 130 ± 40 ms for OFF-type responses. The transience metric, which is used to characterize the sustained nature of the network activation in response to light stimulus, revealed that ON-type responses have a transience of 43 ± 24 ms, while OFF-type responses exhibited a shorter transience of 23 ± 20 ms. The average latency of activation for electrical stimulation across all experiments was 2.1 ± 0.5 ms for the first spiking and 4.1 ± 2.1 ms for peak spiking responses (see Experimental for further description of the mentioned metrics). Statistical tests revealed that first spiking and peak spiking behaviour are significantly different within each tested group (Mann–Whitney–Wilcoxon, $p < 10^{-4}$). The three response categories reveal significant differences when compared for first and peak spiking latencies (Mann–Whitney–Wilcoxon, $p < 10^{-4}$).

In the literature on epiretinal stimulation, multiple mechanisms have been described for the activation of RGCs. These mechanisms include a short-latency spiking period (up to 7 ms), hypothesized to originate from direct activation, and a longer-latency spiking period (up to a few hundred ms) resulting from presynaptic activation, which induces a burst of action potentials.[18,25,46–48] Based on our findings regarding latencies for electrical stimulation, we conclude that the rGO microelectrodes are capable of directly activating the RGCs. Conversely, latencies measured for light stimulation confirm that, as anticipated, light activates the entire retinal circuitry, thereby causing indirect activation.

We further explored the electrical stimulation parameters that elicit a retinal response. Fig. 4e presents the strength-duration curve for a 25 μm diameter electrode, where currents of a few microamps are needed to induce a response. We observed threshold charge densities between 0.36 and 0.51 mC cm^{-2} (total charge range: 1.79–2.53 nC) for the 490.64 μm^2 electrodes. These values generally align with the literature on activation thresholds for retinal neurons (refer to ref. 25 for a summary of thresholds) and closely replicate those reported by Wyatt *et al.*[49] and Rizzo *et al.*,[50] who used electrodes of similar size and pulse widths, reporting 0.29 mC cm^{-2} and 0.33 mC cm^{-2}, respectively. Employing a power fit, rheobase and chronaxie were calculated as 1.48 μA and 0.88 ms, respectively, in agreement with previously reported data from different species (monkey, guinea pig, and rats).[25] To determine the most accurate fit, three different fitting functions were tested: exponential (R^2 = 0.789), Lapicque (R^2 = 0.853), and power (R^2 = 0.998). The power fit provided the best results, consistent with findings reported in the literature.[25]

We analyzed the activation profiles of the RGCs in response to varying current injections by applying kernel density functions to the PSTH for the initial 40 ms following stimulus delivery. This approach enabled us to quantify differences in the induced repeated firing activity, referred to as activation strength, as depicted in Fig. 4f (see Experimental for a detailed

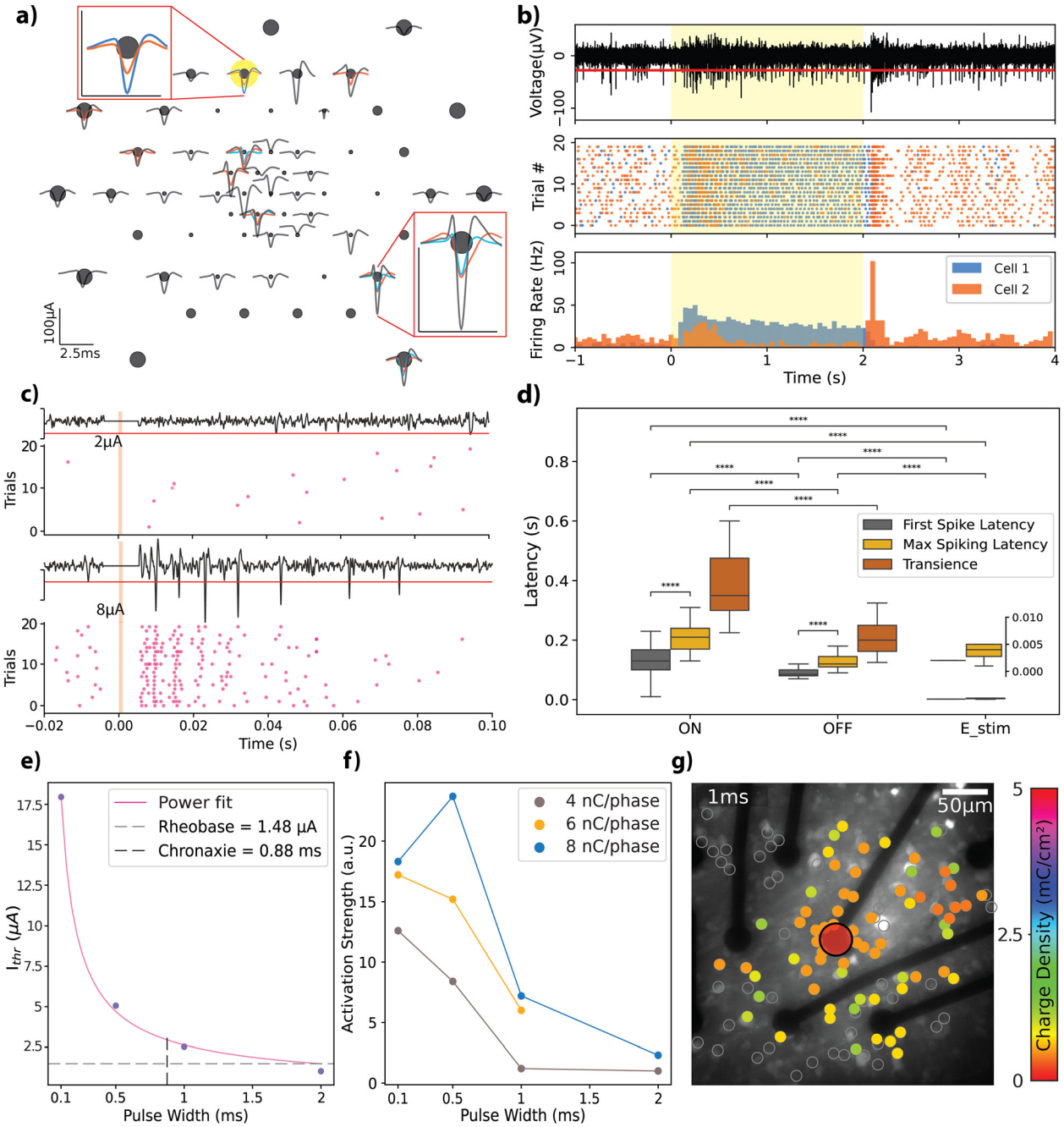

Fig. 4 *Ex vivo* retinal recording and stimulation with rGO microelectrodes. (a) Depiction of light-evoked action potentials, following spike sorting, from a retinal explant recorded by the rGO MEA in response to 450 nm full-field LED presentations. Insets show zoomed-in spike shapes from select channels; scale bars in the insets are depicted matching the magnitudes given in the original image. (b) LED stimulation trials recorded by one of the highlighted electrodes in panel a, where the yellow window indicates the stimulation period. A trace snippet from the last trial of the presented experiment is visible in the top segment, with the red line denoting the 6 MAD threshold. Spiking response over a given experiment is depicted in raster plots (middle row) and PSTH (bottom row). Two neural units with distinct characteristics were observed (cell 1: purple, cell 2: orange) where cell 1 exhibits an ON-type response whereas cell 2 exhibits an OFF-type response. (c) RGC response dynamics for 2 µA and 8 µA cathodic-first charge-balanced biphasic current stimulation (500 µs pulse width) recorded by an electrode 150 µm away from the stimulation electrode (size: 25 µm). Orange window depicts the duration of electrical stimulation. (d) Temporal activation dynamics for light and electrical stimulation experiments. Latency and transience for light stimulation and latency for electrical stimulation is shown (Mann–Whitney–Wilcoxon, ****: $p < 10^{-4}$). Inset shows a zoom-out for the electrical stimulation experiments. (e) Strength duration curve extracted from the electrical stimulation experiments. (f) Activation strength of the retinal circuitry for charge injections of 4 nC, 6 nC, and 8 nC per phase delivered during different time windows as given in the *x*-axis. (g) Spatial mapping of the RGC activation in the field of view with a 1 ms pulse width and injected charge densities between 0–5 mC cm^{-2}. Color bar represents the threshold charge densities for each cell that is highlighted with grey circles.

description). This metric facilitated the comparison of activation dynamics across different combinations of amplitude and pulse widths, each leading to equal total injected charges of 4 nC, 6 nC, or 8 nC per phase at the interface. Obtained trends indicate that the strength of activation decreases as the pulse width is increased. Ahuja *et al.* reported that total charge injected was a more critical factor for initiating retinal excitation than charge density across an electrode.[48] Our study adds a new perspective by confirming the significance of the time course of the injected charge. We demonstrated that shorter pulse widths can produce more robust activation at the same charge amount.

The spatial extent of RGC activation was tracked using calcium imaging (see Fig. S5a and b, ESI†). We analysed the responses of 1110 identified cells to stimulation parameters detailed in Table S2 (ESI†). Fig. 4g shows the threshold charge densities for cells that responded to biphasic current injections of 1 ms pulse width. Here we stimulated the cells with a single 25 μm electrode with the previously described charge densities and constructed a heatmap of activation thresholds for the cells in the field of view. The effects of varying the stimulation pulse width are further demonstrated in Fig. S5c and d (ESI†) showing how pulse duration and amplitude influence the spatial resolution of the response in the RGCs. A pulse of 0.1 ms activates cells near the stimulating electrode, while pulses longer than 1 ms induce responses over a broader area. The mean distances of cells responding to specific stimuli, relative to the edge of the 25 μm diameter electrode, were 35 μm for 0.1 ms pulses, 83 μm for 1 ms pulses, and 74 μm for 4 ms pulses (Fig. S5e, ESI†). When applying 0.1 ms pulses, stimulation was confined to the outline of the active electrode (35 μm), activating only a few cells. Therefore, we conclude that short stimulation through our 25 μm rGO electrodes can focally activate cells within the ganglion cell layer.

3 Conclusion

In this study, we developed rGO MEAs for interfacing with neural cultures and explanted retinas. Using a wafer-scale thin-film fabrication process based on reduced graphene oxide porous membranes, we prepared MEAs on glass substrates with electrode diameters of 25 μm, 50 μm, and 100 μm. The electrochemical characterization demonstrated favourable properties, evidenced by low impedance at 1 kHz between ~28 kΩ and ~6 kΩ for electrodes with diameters from 25 μm to 100 μm and high CIL values up to ~4 mC cm^{-2} for 1 ms pulse width, underscoring the material's performance. The importance of using appropriate metrics to compare electrochemical performance cannot be understated.[30] The numerous factors that can influence such measurements make it very challenging to draw direct parallels between different electrode materials. Despite these complexities, it's noteworthy that rGO electrodes demonstrate promising performance based on commonly used figures of merit. Biocompatibility and the mechanical stability of the material were reported in a previous study,[27] supporting their reliability for *in vivo* neural interfacing applications. We would like to emphasize that, while in this study rigid MEAs are employed to conduct *in vitro* electrophysiology, we have also demonstrated the integration of rGO MEAs into flexible substrates for implantable neural interfaces.[27]

We initially used dissociated hippocampal cultures to demonstrate the capabilities of the rGO MEA technology. The progression of cell growth and corresponding electrical activity over a two-week period demonstrated the viability and effectiveness of the rGO MEAs in capturing neural signals. We noted that smaller diameter electrodes recorded larger spike amplitudes, however the SNR was not significantly different between electrode sizes. Retinal explants were employed to further evaluate the bidirectional interfacing capabilities of the rGO MEAs. Light-evoked action potentials recorded from retinal neurons helped categorize neural response dynamics into 'ON-type' or 'OFF-type' responses, providing insights into the biophysical origins of these activities. The rGO MEAs demonstrated effective neural modulation capabilities, with different pulse widths and amplitudes eliciting varying responses with temporal dynamics matching the literature. Calcium imaging experiments further explored the neural modulation capabilities the rGO MEAs by allowing the observation of individual neuronal responses and spatially map the distribution of responses.

We have developed an MEA technology that supports multiple recording sites with bidirectional capability, demonstrating its effectiveness through comprehensive functional testing. Retinal prostheses require high-density electrode arrays for selective activation of retinal neurons. The ability of rGO MEAs to maintain low impedance and high CIL even at microscale dimensions enables the construction of densely packed arrays. This feature is crucial for stimulating the targeted retinal structures with precision, potentially improving the resolution of perceived images by patients. rGO's proven biocompatibility reduces the risk of inflammation, while its mechanical flexibility allows the electrode array to conform closely to the curved retinal surface. This close interface enhances the effectiveness of neural stimulation and signal recording. The bidirectional capability of rGO MEAs enables not only stimulation but also the recording of neural activity. This feature is integral to developing closed-loop retinal prostheses that can dynamically adjust stimulation parameters in real time based on feedback from neural recordings. Such adaptability can lead to more personalized and effective therapies, enhancing the quality of vision restoration. Future research will be necessary to assess the *in vivo* stability and efficacy of these electrodes in chronic implantation scenarios, which is a vital consideration to unlock their full potential for therapeutic applications.

4 Experimental

4.1 Fabrication of rGO MEAs

We fabricated arrays of 60 microelectrodes based on rGO as the material (Fig. 1a). The MEA design included electrode

diameters of 25 μm (n = 31), 50 μm (n = 18) and 100 μm (n = 11) (corresponding geometric surface areas of 490.63 μm^2, 1962.5 μm^2 and 7850 μm^2), as shown in Fig. 1a, bottom panel. We employed three different electrode sizes to investigate the scaling of electrochemical performance with size and to assess functional performance through recording experiments. The 25 μm electrodes were specifically utilized in stimulation experiments to achieve focal activation. The fabrication methodology employed in our study was previously described in ref. 27; a key distinction in our process is the use of rigid substrates (500 μm-thick borosilicate), as opposed to the use of flexible substrates. Briefly, a graphene oxide suspension (Global Graphene Group) of 0.15 mg mL^{-1} was vacuum filtered using an anodisc inorganic filter membrane (Whatman) with pore a size of 0.025 μm to obtain a graphene oxide film approximately 2 μm thick. Following filtration, the thin-film was transferred onto a borosilicate wafer (borofloat33, Planoptik) that was previously sputtered with gold. A hydrothermal reduction step was applied to the GO film to increase the material conductivity. Electrodes were defined by patterning the rGO with reactive ion etching, and the metal tracks were defined by chemically etching the gold layer. Everything except the electrodes was encapsulated with a SU8 resin (Kayaku AM). Scanning electron microscopy (SEM) (Fig. 1b), atomic force microscopy (AFM) (Fig. 1c, left), and Raman spectroscopy (Fig. 1c, right) techniques were employed to characterize the physico-chemical properties of the rGO microelectrodes. SEM images were obtained with a Quanta 650F ESEM (FEI Company), and AFM measurements were conducted using an MFP-3D Origin+ (Oxford Instruments). Raman spectra were obtained using a Witec Alpha300R A300M+ (Oxford Instruments) equipped with 488 nm laser excitation line and a 50× objective and 600 grooves per nm grating. To prevent sample heating, laser power was maintained under 1.5 mW.

Standard electrochemical methods were employed for characterization of the microelectrodes. Electrochemical impedance spectroscopy (EIS), cyclic voltammetry (CV), and chronoamperometry measurements were performed in an aqueous electrolyte (10 mM PBS, total ion concentration 15 mM) using a potentiostat (PGSTAT128N, Metrohm AUTOLAB) in 3-electrode configuration. EIS measurements used a 10 mV sinusoidal excitation over a 1 Hz–100 kHz range, with 5 samples per decade (Fig. 2a). A transmission line-like model (see Fig. 2b), comprising only a combination of resistors (R) and capacitors (C), was employed to model the frequency response of the rGO microelectrodes. R and C values were extracted for each electrode after fitting the model with ZView 4 (Scribner). The NRMSE of the fitted parameters was computed by first determining the root mean square error (RMSE) normalized by the range of the measured data, defined as the difference between the maximum and minimum measured values. The NRMSE values were computed for each electrode within the grouped data.

CV traces were recorded for 50, 100, 200, and 500 mV s^{-1} scan rates within the identified electrochemical window of −0.9 to +0.8 V (*versus* Ag/AgCl). Fig. 2c shows results from the measurements at 50 mV s^{-1} scan rate, presented as current density *versus* potential, normalized by the surface area. Cathodic charge storage capacity (CSCc) for the electrodes was calculated by integrating the area under the cathodic half of the 50 mV s^{-1} CV curves, as described in the literature[30] (Fig. 2d). Chronoamperometry measurements were conducted using charge-balanced cathodic-first biphasic current injections of 1 ms per phase for amplitudes between 5–25 μA (25 μm), 5–40 μA (50 μm) and 5–100 μA (100 μm). Representative traces from an electrode of 25 μm diameter is depicted in Fig. 2e.

Polarization across the interface for different electrode diameters was shown *versus* injected current amplitudes in Fig. 2f. The CIL, which is used as a figure of merit of electrode performance, was extracted by calculating the charge density at the maximum current amplitude that does not cause the potential difference at the interface to exceed the water window (Fig. 2g).

4.2 Functional testing on hippocampal neurons in culture

All animal procedures were conducted in accordance with standard ethical guidelines (European Communities Directive 86/609/EU) and were approved by the local ethical committees. Primary embryonic rat hippocampal neurons were isolated from E18 Sprague Dawley embryos (Harlan Laboratories Ltd). Isolated hippocampi were enzymatically digested in 0.5 mg mL^{-1} papain (P4762, Sigma-Aldrich) and 0.01 mg mL^{-1} Deoxyribonuclease (D5025-15KU, Sigma-Aldrich) in PBS supplemented with 0.5 mg mL^{-1} Bovine Serum Albumin (11020021, Thermo Fisher Scientific) and 10 mM D-(+)-glucose (G5400, Sigma-Aldrich) for 30 min at 37 °C. Subsequently from enzymatic digestion, hippocampi were washed once with 10% (v/v) heat-inactivated FBS (F2442, Sigma Aldrich) in Neurobasal Plus medium (A3582901, Thermo Fisher Scientific) and twice with Neurobasal Plus medium. Tissue fragments were then mechanically dissociated with a 5 mL serological pipette and filtered with a 40 μm strainer (CSS013040, Biofil). The cells were seeded at a concentration of 250 000–300 000 cells per cm and kept in an incubator at 37 °C and 5% CO_2 with culture media: 89% DMEM (Life Technologies), 1% Pen/Strep (Life Technologies), and 10% FBS. Cellular growth was followed up by recording spontaneous activity with the MEA2100-Mini-System (Multichannel Systems GmbH) from the cultures at different time points (Fig. 3a and b).

Biphasic, charge-balanced voltage pulses of varying intensities (400–900 mV) (Fig. 3d) and durations (300–900 μs) (Fig. S3d, ESI†) were applied to test the neural activity modulation capabilities of our MEAs. The pulses were separated by a resting period of 10 seconds and were repeated between 5–10 times. Intracellular calcium changes were used as evidence of neural activity modulation upon delivery of the voltage pulses (Fig. 3e). Cultures of hippocampal neurons were incubated with ssAAV-DJ/2-hSyn1-jGCaMP8m-WPRE-SV40p (Janelia) (titer 5×10^{10} GC per mL) at 2 DIV. Cultures were left to mature and, at 16 DIV, calcium activity evoked by electrical stimulation was recorded with a confocal microscope (FluoView3000, Olympus) equipped with a 10 × 0.30 air objective (UPLFLN, Olympus), an incorporated incubator and a MEA recording/stimulation system (MEA2100-Mini-System,

Multichannel Systems GmbH) (see Fig. S2, ESI†). Fluorescence from the GCaMP8m was excited with a 488 nm argon laser and the emission was collected with a GaAsp detector at 1.86 fps.

4.3 Modulation of neural activity on retinal explants

Long-Evans rats were deeply anaesthetized with 35% CO_2 inhalation, and the CO_2 concentration was increased to 70% for euthanasia. The eyes were enucleated, and the retinas were dissected in oxygenated (95% O_2/5% CO_2) Ames media (A1420, Sigma-Aldrich) adjusted to pH 7.4 and 280 mOsm. The vitreous was carefully removed with a pair of tweezers, and four cuts were made to allow the retina to flatten completely. Each retina was flat-mounted with the ganglion cell layer (GCL) facing up on a porous membrane (JVWP01300, Merckmillipore) attached to a metallic ring. This assembly was then inverted on top of the MEA, positioning the GCL directly on the rGO electrodes. During the course of the experiment, the sample was infused with oxygenated fresh Ames' medium at a flow rate of 5 mL min^{-1} at 33 °C using a custom-made system (see ref. 51 for a detailed description).

Neural activity was recorded at a 25 kHz sampling rate, upon electrical and light stimulation using the MEA2100-Mini-System (Multichannel Systems GmbH). Light stimulation of the retina was performed after dark adapting the retina for 5 minutes. Retinas were stimulated with 2-second pulses of 450 nm full-field LED light focused on the center of the retina section using a computer-controlled monochromator (Polychrome V, TILL Photonics). Each trial consisted of 20 light pulses delivered with an inter-pulse gap of 11 seconds (see Fig. 4b). To block the ON response, the retina was perfused for 15 minutes with 50 μM L-AP4 (Tocris). After L-AP4 perfusion, the light stimulation protocol was repeated (Fig. S4a, ESI†). Current-controlled, biphasic, cathodic-first stimulation was delivered through a STG-2008 stimulus generator (Multichannel Systems GmbH). Single charge-balanced biphasic current injections of 0.1, 0.5, 1, and 2 ms pulse widths without inter-phase gap, combined with the appropriate amplitudes between 1–40 μA (see Table S1, ESI†) were used which consisted of 20 pulses per trial with 12 second inter-pulse gap (Fig. 4c). A silver/silver–chloride pellet immersed in the solution served as a distant monopolar return electrode.

For visualizing the calcium activity from the GCL of rat retina explants, animals were intravitreally injected with adeno-associated viral (AAV) particles carrying a genetically encoded fluorescent calcium indicator (AAV2-CAG-GCaMP5G). Animals were monitored before and 10–17 days after injection for *in vivo* assessment of retinal structure and AAV-derived fluorescence expression by fundoscopy and optical coherent tomography (OCT) using the Micron III platform (Phoenix Research Laboratories). During *in vivo* imaging, animals were kept under Isoflurane anaesthesia and on a heating pad. Pupils were dilated with Tropicamide. Phenylephrine (100 mg mL^{-1}, Alcon Cusí Laboratories) was applied as a local anaesthetic and 2% Methocel gel (OmniVision) was administered to facilitate better contact between the Micron III lens and the cornea. Calcium activity was monitored while delivering single charge-balanced biphasic current pulses with a custom-built ASIC system (Fig. 4g and Fig. S5c, d, e, ESI†). Single charge-balanced biphasic current injections of 0.1, 1, and 4 ms pulse widths with 100 ms inter-phase gap, combined with the appropriate amplitudes between 0.15–30 μA (see Table S2, ESI†) were used which consisted of 4 pulses per trial with 1 ms inter-pulse gap. Each stimulation trial occured every 10 seconds for a minute of calcium imaging recording.

4.4 Data analysis

Electrophysiological data were processed using custom-built scripts in Python v3.10, utilizing libraries such as Numpy, Pandas, SciPy, Elephant, SpikeInterface, Seaborn, Matplotlib, Statmodels, Statannot. Data conversion was performed using tools and libraries provided by Multi-Channel Systems. The scaled signals were then bandpass filtered with a 2nd-order IIR Butterworth filter between 300 Hz and 3 kHz.[52] Phase distortion caused by the filter was corrected using a forward-backward filtering strategy. Electrical stimulation artifacts were removed by examining the change in the derivative of the filtered signal using a moving average thresholding strategy.

Spike detection was performed using an automatic median absolute deviation (MAD) threshold set at 6*MAD, combined with a 2.5 ms refractory period window (up to 5 ms refractoriness).[53] A 2.4 ms window around the identified peak was extracted and oversampled (4×) using cubic spline interpolation and peak points were centered within the window and downsampled to the original sampling rate to avoid temporal jitter. The signal-to-noise ratio (SNR) was determined by dividing the average peak-to-peak amplitude of detected spikes for each channel by the standard deviation of the baseline signal. The results were then reported on a decibel (dB) scale using $20\log 10(V_{p-p}/V_{STD})$ (Fig. 3c). This calculation was performed exclusively on channels that exhibited spontaneous activity. Dimensionality reduction was performed using principal component analysis to the extracted candidate spikes of the same session, and selecting n dimensions which contained at least 80% of the original signal content. Spikes were registered by further analysis with k-means clustering, in which the clusters were identified as a spike by visual inspection of the averaged shape of each cluster.

In addition to the analysis with custom scripts, SpikeInterface library[54] was employed for applying multiple established sorting algorithms. A sparse sorting method was employed, where a sorted unit is registered only on the channel that shows the largest amplitude was used. Identified units, as shown in Fig. 4a, were further analysed for activation latency per response type (ON, OFF and electrical stimulation). Timestamps were extracted using peristimulus time histograms (PSTH) with a bin size of 10 ms from two distinct spiking responses: ''first spiking'' and ''peak spiking''. The ''first spiking'' response is defined as the moment within the stimulus onset window when the spike count surpasses the maximum observed during the baseline period. Conversely, ''peak spiking'' is identified as the point at which the maximum response is recorded. Transience, or the response decay time, was

defined as the timepoint where response decreased to 1/*e* of its maximum value (see Fig. 4d). Maximum spiking numbers were extracted from the first 10 ms after stimulation with a PSTH of 1 ms bin width.

Firing probability for each pulse width *versus* amplitude was calculated by normalizing the PSTH counts to the maximum spike count, with thresholds set at 50% probability (see Fig. S6, ESI†). Strength-duration data were plotted using the calculated thresholds; rheobase and chronaxie were determined by fitting a power function to the strength-duration data (Fig. 4e). We tested three different fitting functions and chose the power function as it provided the best fit, as evidenced by the fitting results: exponential (R^2 = 0.789), Lapicque (R^2 = 0.853), and power (R^2 = 0.998). Furthermore, a metric was developed to quantify the complex response of the retinal neurons in electrical stimulation experiments. This was achieved by applying kernel density functions to the first 400 ms of the retinal response histograms and then calculating the area under the curve, which represents the activation strength in arbitrary units (see Fig. S7, ESI†). This metric was calculated for each stimulation amplitude and pulse width combination which allowed us to quantify the difference in activation dynamics with respect to the total injected charge within different temporal windows. Finally, obtained activation strength values were plotted with respect to pulse widths categorized by total charge injected per phase (Fig. 4f). Datapoints were connected with lines to facilitate the interpretation of the trends.

The calcium imaging data upon electrical stimulation was analyzed as follows. Fluorescence intensity profiles from each cell body were obtained after manual image segmentation using FIJI (ImageJ, version 1.50i). Cells were manually segmented by defining regions of interest (ROIs) on the corresponding bright field images. The average fluorescence intensity for each ROI was measured at successive time points using the ''Measure'' function in ImageJ's ROI Manager. Fluorescence intensity profiles from cell cultures, along with the size and position of each ROI, were then imported into Python. A polynomial fit was applied to correct for any photobleaching effects in the fluorescence data. Non-stimulation periods were used to calculate the baseline signal. Spike detection was based on the criterion that the fluorescence intensity of a ROI had to be at least 2.75 times higher than the baseline intensity at any given time point. Subsequently, data from the stimulator were imported and synchronized with the fluorescence recordings. Relative stimulation efficacy was calculated by dividing the number of stimuli that triggered a spike by the total number of stimuli administered (Fig. 3f). This efficacy was visually represented in a grid plot, with each pixel corresponding to a specific ROI, thereby providing a comprehensive overview of the stimulation effects across the neuronal network.

Fluorescence intensity profiles from RGCs were processed following the same criteria using a custom-built script in MATLAB (Version R2021b, MathWorks) that automatically categorizes cells as responding or unresponsive.[51] The coordinates of ROIs were used to calculate the distance from the responding cells to the electrode providing the stimuli. To do so, we applied the distance formula of the Pythagorean theorem:

$$d = \sqrt{(x_2 - x_1)^2 + (y_2 - y_1)^2}$$

and subtracted the diameter of the active electrode. The boxplot was generated using GraphPad Prism (version 9.3.1, GraphPad Software).

To investigate statistical significance, we conducted normality and homogeneity tests to determine whether to use parametric or non-parametric methods. This was followed by applying the appropriate statistical and *post hoc* tests for the analysis of the reported parameters. All reported averages are presented as mean ± standard deviation format.

Author contributions

Conceptualization: J. A. G., S. P., P. L. A., M. Chme., S. D.; data curation: F. T. D., M. Cun.; investigation: D. V., D. N., J. M. D. C., M. Cun., S. T. W., M. Cun., F. T. D., M. M.; formal analysis: F. T. D., M. Cun.; resources: J. D., X. I., J. M. Z., M. P. B., J. G. M. M., C. P., G. C. O., E. D. C.; visualization: F. T. D., M. Cun.; writing-original draft: F. T. D., M. Cun., E. M. C.; writing-review & editing: F. T. D., E. M. C., J. A. G., S. T. W., S. P., M. Cun., M. M., P. L. A., S. D.

Data availability

Data will be made available upon request by contacting the authors.

Conflicts of interest

There are no conflicts to declare.

Acknowledgements

The project leading to these results have received funding from ''la Caixa'' Foundation (ID 100010434), under the agreement LCF/PR/HR19/52160003 (i-VISION), European Unions Horizon 2020 research and innovation programme under grant agreement no. 881603 (Graphene flagship Core3), and French state funds managed by the Agence Nationale de la Recherche (ANR) within Programme Investissements dAvenir, Laboratoire dExcellence (LABEX) LIFESENSES (ANR-10-LABX-0065) and Institut Hospitalo-Universitaire FOReSIGHT (ANR-18-IAHU-0001). We also acknowledge funding from the Generalitat de Catalunya (2021SGR001534). E. D. C. thanks the Ayuda RYC2019-027879-I founded by MCIU/AEI/10.13039/501100011033 and by El FSE invierte en tu futuro. E. M. C. acknowledges Ayuda FJC2021-046601-I financiada por MCIU/AEI/10.13039/501100011033 y por la Unión Europea NextGenerationEU/PRTR. This research was funded by the Spanish Ministerio de Ciencia e Innovación (PID2020-113663RB-I00) founded by (MCIU/AEI/10.13039/501100011033) and by ''ERDF A way of making Europe''. The ICN2 has been supported by the Severo Ochoa Centres of Excellence programme [SEV-2017-0706] and is

currently supported by the Severo Ochoa Centres of Excellence programme, Grant CEX2021-001214-S, both funded by MCIN and MCIU/AEI/10.13039.501100011033. This project has also received funding from the European Unions Horizon 2020 research and innovation programme under the Marie Skłodowska-Curie grant agreement no. 861423 (enTRAIN Vision). Part of this work was performed at the Spanish ICTS Network MICRONANOFABS partially supported by MICINN, and the ICTS 'NANBIOSIS', more specifically by the Micro-Nano-Technology Unit of the CIBER in Bioengineering, Biomaterials and Nanomedicine (CIBER-BBN) at the IMB-CNM. DN has received funding from the doctoral school of Cerveau, cognition, comportement (3C) at Sorbonne Université.

Notes and references

1 S. Y. Kim, S. Sadda, J. Pearlman, M. S. Humayun, E. De Juan, B. M. Melia and W. R. Green, *Retina*, 2002, **22**, 471–477.
2 B. W. Jones, R. L. Pfeiffer, W. D. Ferrell, C. B. Watt, M. Marmor and R. E. Marc, *Exp. Eye Res.*, 2016, **150**, 149–165.
3 J. H. Wong, J. Y. Ma, A. I. Jobling, A. Brandli, U. Greferath, E. L. Fletcher and K. A. Vessey, *Front. Neurosci.*, 2022, **16**, 1–21.
4 M. S. Humayun, E. De Juan, G. Dagnelie, R. J. Greenberg, R. H. Propst and D. H. Phillips, *Arch. Ophthalmol.*, 1996, **114**, 40–46.
5 L. Da Cruz, B. F. Coley, J. Dorn, F. Merlini, E. Filley, P. Christopher, F. K. Chen, V. Wuyyuru, J. Sahel, P. Stanga, M. Humayun, R. J. Greenberg and G. Dagnelie, *Br. J. Ophthalmol.*, 2013, **97**, 632–636.
6 K. Stingl, K. U. Bartz-Schmidt, D. Besch, A. Braun, A. Bruckmann, F. Gekeler, U. Greppmaier, S. Hipp, G. Hortdorfer, C. Kernstock, A. Koitschev, A. Kusnyerik, H. Sachs, A. Schatz, K. T. Stingl, T. Peters, B. Wilhelm and E. Zrenner, *Proc. R. Soc. B*, 2013, **280**, 1–8.
7 L. Yue, J. D. Weiland and M. S. Humayun, in *Retinal Prostheses: A Brief History*, ed. M. S. Humayun and L. C. Olmos de Koo, Springer International Publishing, Cham, 2018, pp. 1–22.
8 M. S. Humayun, J. D. Dorn, L. da Cruz, G. Dagnelie, J.-A. Sahel, P. E. Stanga, A. V. Cideciyan, J. L. Duncan, D. Eliott, E. Filley, A. C. Ho, A. Santos, A. B. Safran, A. Arditi, L. V. Del Priore and R. J. Greenberg, *Ophthalmology*, 2012, **119**, 779–788.
9 E. Bloch, Y. Luo and L. da Cruz, *Ther. Adv. Ophthalmol.*, 2019, **11**, 251584141881750.
10 D. Palanker, Y. Le Mer, S. Mohand-Said and J. A. Sahel, *Nat. Commun.*, 2022, **13**, 1–6.
11 K. Stingl, K. U. Bartz-Schmidt, D. Besch, C. K. Chee, C. L. Cottriall, F. Gekeler, M. Groppe, T. L. Jackson, R. E. MacLaren, A. Koitschev, A. Kusnyerik, J. Neffendorf, J. Nemeth, M. A. N. Naeem, T. Peters, J. D. Ramsden, H. Sachs, A. Simpson, M. S. Singh, B. Wilhelm, D. Wong and E. Zrenner, *Vision Res.*, 2015, **111**, 149–160.
12 T. B. Esler, R. R. Kerr, B. Tahayori, D. B. Grayden, H. Meffin and A. N. Burkitt, *PLoS One*, 2018, **13**, 1–27.
13 H. Kasi, W. Hasenkamp, G. Cosendai, A. Bertsch and P. Renaud, *J. NeuroEng. Rehab.*, 2011, **8**, 1–10.
14 D. K. Freeman and S. I. Fried, *J. Neural Eng.*, 2011, **8**, 016008.
15 C. De Balthasar, S. Patel, A. Roy, R. Freda, S. Greenwald, A. Horsager, M. Mahadevappa, D. Yanai, M. J. McMahon, M. S. Humayun, R. J. Greenberg, J. D. Weiland and I. Fine, *Invest. Ophthalmol. Visual Sci.*, 2008, **49**, 2303–2314.
16 A. P. Fornos, J. Sommerhalder, L. da Cruz, J. A. Sahel, S. Mohand-Said, F. Hafezi and M. Pelizzone, *Invest. Ophthalmol. Visual Sci.*, 2012, **53**, 2720–2731.
17 A. C. Weitz, D. Nanduri, M. R. Behrend, A. Gonzalez-Calle, R. J. Greenberg, M. S. Humayun, R. H. Chow and J. D. Weiland, *Sci. Transl. Med.*, 2015, **7**, 1–12.
18 S. I. Fried, H. A. Hsueh and F. S. Werblin, *J. Neurophysiol.*, 2006, **95**, 970–978.
19 D. Nanduri, I. Fine, A. Horsager, G. M. Boynton, M. S. Humayun, R. J. Greenberg and J. D. Weiland, *Invest. Ophthalmol. Visual Sci.*, 2012, **53**, 205.
20 A. G. Habib, M. A. Cameron, G. J. Suaning, N. H. Lovell and J. W. Morley, *J. Neural Eng.*, 2013, **10**, 036013.
21 C. Y. Yang, D. Tsai, T. Guo, S. Dokos, G. J. Suaning, J. W. Morley and N. H. Lovell, *J. Neural Eng.*, 2018, **15**, 046020.
22 Y. C. Chang, D. H. Ghaffari, R. H. Chow and J. D. Weiland, *J. Neural Eng.*, 2019, **16**, 345–348.
23 L. E. Grosberg, K. Ganesan, G. A. Goetz, S. S. Madugula, N. Bhaskhar, V. Fan, P. Li, P. Hottowy, W. Dabrowski, A. Sher, A. M. Litke, S. Mitra and E. J. Chichilnisky, *J. Neurophysiol.*, 2017, **118**, 1457–1471.
24 R. Dinyari, J. D. Loudin, P. Huie, D. Palanker and P. Peumans, *Technical Digest – International Electron Devices Meeting*, IEDM, 2009, pp. 595–598.
25 C. Sekirnjak, P. Hottowy, A. Sher, W. Dabrowski, A. M. Litke and E. J. Chichilnisky, *J. Neurophysiol.*, 2006, **95**, 3311–3327.
26 H. A. Shah, S. R. Montezuma and J. F. Rizzo, *Exp. Eye Res.*, 2006, **83**, 247–254.
27 D. Viana, S. T. Walston, E. Masvidal-Codina, X. Illa, B. Rodríguez-Meana, J. del Valle, A. Hayward, A. Dodd, T. Loret, E. Prats-Alfonso, N. de la Oliva, M. Palma, E. del Corro, M. del Pilar Bernicola, E. Rodríguez-Lucas, T. Gener, J. M. de la Cruz, M. Torres-Miranda, F. T. Duvan, N. Ria, J. Sperling, S. Martí-Sánchez, M. C. Spadaro, C. Hébert, S. Savage, J. Arbiol, A. Guimerà-Brunet, M. V. Puig, B. Yvert, X. Navarro, K. Kostarelos and J. A. Garrido, *Nat. Nanotechnol.*, 2024, 1–10.
28 J. A. López-Villanueva and S. Rodríguez Bolívar, *Energies*, 2022, **15**, 792.
29 S. F. Cogan, *Annu. Rev. Biomed. Eng.*, 2008, **10**, 275–309.
30 J. W. Gittins, Y. Chen, S. Arnold, V. Augustyn, A. Balducci, T. Brousse, E. Frackowiak, P. Gómez-Romero, A. Kanwade, L. Köps, P. K. Jha, D. Lyu, M. Meo, D. Pandey, L. Pang, V. Presser, M. Rapisarda, D. Rueda-García, S. Saeed, P. M. Shirage, A. Slesinski, F. Soavi, J. Thomas, M. M. Titirici, H. Wang, Z. Xu, A. Yu, M. Zhang and A. C. Forse, *J. Power Sources*, 2023, **585**, 233637.
31 J. D. Weiland, D. J. Anderson and M. S. Humayun, *IEEE Trans. Biomed. Eng.*, 2002, **49**, 1574–1579.
32 A. Ghazavi, J. Maeng, M. Black, S. Salvi and S. F. Cogan, *J. Neural Eng.*, 2020, **17**, 016022.

33 A. Weremfo, P. Carter, D. B. Hibbert and C. Zhao, *Langmuir*, 2015, **31**, 2593–2599.
34 R. Gerwig, K. Fuchsberger, B. Schroeppel, G. S. Link, G. Heusel, U. Kraushaar, W. Schuhmann, A. Stett and M. Stelzle, *Front. Neuroeng.*, 2012, **5**, 1–11.
35 S. J. Wilks, S. M. Richardson-Burns, J. L. Hendricks, D. C. Martin and K. J. Otto, *Front. Neuroeng.*, 2009, **2**, 1–8.
36 R. A. Green, P. B. Matteucci, R. T. Hassarati, B. Giraud, C. W. Dodds, S. Chen, P. J. Byrnes-Preston, G. J. Suaning, L. A. Poole-Warren and N. H. Lovell, *J. Neural Eng.*, 2013, **10**, 016009.
37 M. Bianchi, A. De Salvo, M. Asplund, S. Carli, M. Di Lauro, A. Schulze-Bonhage, T. Stieglitz, L. Fadiga and F. Biscarini, *Adv. Sci.*, 2022, **9**, 1–30.
38 M. A. Hejazi, W. Tong, A. Stacey, S. H. Sun, M. Yunzab, A. Almasi, Y. J. Jung, H. Meffin, K. Fox, K. Edalati, A. Nadarajah, S. Prawer, M. R. Ibbotson and D. J. Garrett, *Adv. Funct. Mater.*, 2020, **30**, 1–10.
39 Y. Nam, D. W. Branch and B. C. Wheeler, *Biosens. Bioelectron.*, 2006, **22**, 589–597.
40 M. Cunquero, E. Aguilar, P. Loza-Alvarez and J. Planagumà, *J. Visualized Exp.*, 2022, 1–18.
41 L. A. Camuñas-Mesa and R. Q. Quiroga, *Neural Comput.*, 2013, **25**, 1191–1212.
42 M. E. J. Obien, K. Deligkaris, T. Bullmann, D. J. Bakkum and U. Frey, *Front. Neurosci.*, 2015, **9**, 423.
43 G. Czanner, S. V. Sarma, D. Ba, U. T. Eden, W. Wu, E. Eskandar, H. H. Lim, S. Temereanca, W. A. Suzuki and E. N. Brown, *Proc. Natl. Acad. Sci. U. S. A.*, 2015, **112**, 7141–7146.
44 A. Suarez-Perez, G. Gabriel, B. Rebollo, X. Illa, A. Guimerà-Brunet, J. Hernández-Ferrer, M. T. Martínez, R. Villa and M. V. Sanchez-Vives, *Front. Neurosci.*, 2018, **12**, 1–12.
45 W. B. Thoreson and J. S. Ulphani, *Brain Res.*, 1995, **676**, 93–102.
46 L. Li, Y. Hayashida and T. Yagi, *Vision Res.*, 2005, **45**, 263–273.
47 R. J. Jensen, O. R. Ziv and J. F. Rizzo, *J. Neural Eng.*, 2005, **2**, S16.
48 A. K. Ahuja, M. R. Behrend, M. Kuroda, M. S. Humayun and J. D. Weiland, *IEEE Trans. Biomed. Eng.*, 2008, **55**, 1744–1753.
49 J. Wyatt, J. Rizzo, A. Grumet, D. Edell and R. Jensen, *Invest. Ophthalmol. Visual Sci.*, 1994, **35**, 1380.
50 J. F. Rizzo and J. Wyatt, *Neuroscientist*, 1997, **3**, 251–262.
51 M. Cunquero, M. Marsal, G. Castro-Olvera, S. T. Walston, F. T. Duvan, J. G. Macias-Montero, C. Puigdengoles, M. Chmeissani, J. A. Garrido and P. Loza-Alvarez, *J. Visualized Exp.*, 2023, **2023**, 1–15.
52 H. G. Rey, C. Pedreira and R. Quian Quiroga, *Brain Res. Bull.*, 2015, **119**, 106–117.
53 M. J. Berry and M. Meister, *Adv. Neural Inform. Process. Syst.*, 1998, **18**, 110–116.
54 A. P. Buccino, C. L. Hurwitz, S. Garcia, J. Magland, J. H. Siegle, R. Hurwitz and M. H. Hennig, *eLife*, 2020, **9**, 1–24.